



UNIVERSITY OF LEEDS

This is a repository copy of *Complementary hydro-mechanical coupled finite/discrete element and microseismic modelling to predict hydraulic fracture propagation in tight shale reservoirs*.

White Rose Research Online URL for this paper:

<http://eprints.whiterose.ac.uk/90979/>

Version: Accepted Version

---

**Article:**

Profit, M, Dutko, M, Yu, J et al. (3 more authors) (2016) Complementary hydro-mechanical coupled finite/discrete element and microseismic modelling to predict hydraulic fracture propagation in tight shale reservoirs. Computational Particle Mechanics, 3 (2). pp. 229-248. ISSN 2196-4378

<https://doi.org/10.1007/s40571-015-0081-4>

---

**Reuse**

Unless indicated otherwise, fulltext items are protected by copyright with all rights reserved. The copyright exception in section 29 of the Copyright, Designs and Patents Act 1988 allows the making of a single copy solely for the purpose of non-commercial research or private study within the limits of fair dealing. The publisher or other rights-holder may allow further reproduction and re-use of this version - refer to the White Rose Research Online record for this item. Where records identify the publisher as the copyright holder, users can verify any specific terms of use on the publisher's website.

**Takedown**

If you consider content in White Rose Research Online to be in breach of UK law, please notify us by emailing [eprints@whiterose.ac.uk](mailto:eprints@whiterose.ac.uk) including the URL of the record and the reason for the withdrawal request.

# Complementary Hydro-Mechanical Coupled Finite/Discrete Element and Microseismic Modelling to Predict Hydraulic Fracture Propagation in Tight Shale Reservoirs

Matthew Profit • Martin Dutko •

Jianguo Yu • Sarah Cole

Doug Angus • Alan Baird

**Abstract** This paper presents a novel approach to predict the propagation of hydraulic fractures in tight shale reservoirs. Many hydraulic fracture modelling schemes assume that the fracture direction is pre-seeded in the problem domain discretization. This is a severe limitation as the reservoir often contains large numbers of pre-existing fractures that strongly influence the direction of the propagating fracture. To circumvent these shortcomings a new fracture modelling treatment is proposed where the introduction of discrete fracture surfaces is based on new and dynamically updated geometrical entities rather than the topology of the underlying spatial discretization. Hydraulic fracturing is an inherently coupled engineering problem with interactions between fluid flow and fracturing when the stress state of the reservoir rock attains a failure criterion. This work follows a staggered hydro-mechanical coupled finite/discrete element approach to capture the key interplay between fluid pressure and fracture growth. In field practice the fracture growth is hidden from the design engineer and microseismicity is often used to infer hydraulic fracture lengths and directions. Microseismic output can also be computed from changes of the effective stress in the geomechanical model and compared against field microseismicity. A number of hydraulic fracture numerical examples are presented to illustrate the new technology.

**Keywords** Hydraulic fracture • Finite/Discrete element method • Coupled geomechanical • Microseismicity

---

M. Profit • M. Dutko • J. Yu • S. Cole  
Rockfield Software Limited, Swansea, SA1 8AS, UK.  
email: [m.dutko@rockfield.co.uk](mailto:m.dutko@rockfield.co.uk)

D. Angus  
University of Leeds, Leeds, UK.  
email: [d.angus@leeds.ac.uk](mailto:d.angus@leeds.ac.uk)

A. Baird  
University of Bristol, Bristol, UK.  
email: [alan.baird@bristol.ac.uk](mailto:alan.baird@bristol.ac.uk)

## 1. Introduction

Hydraulic fracturing is an engineering process often used by the petroleum industry to extract hydrocarbons from very low porosity reservoir rock which would otherwise be economically unviable [1,2,3,4,5,6]. The use of numerical models in the design stage would be an advantageous tool to optimise the hydrocarbon recovery for a given tight shale reservoir. Standard practice in the industry often assumes equal spacing between stimulation points [2] and for reservoirs with local variations in stress and material properties, this may be sub-optimal leading to significantly reduced ultimate recovery of hydrocarbons.

A key design variable in hydraulic fracturing is the stimulated reservoir volume (SRV) [7] and its value is a complex function of, amongst others, shale material properties, pump rates of fracking fluids in both clean and proppant laden states, the initial stress state and the density of natural fractures in the reservoir. Given the number of interacting mechanisms it is no surprise that empirical formulations provide only a limited guide on the relationship between injected fluid and the resulting SRV.

The petroleum industry has focused its efforts in many directions to provide quantitative information between key design variables such as the type and rate of fluid injected and the final SRV. These can be broadly broken into four main categories: empirical, analytical, semi-analytical and numerical methods. Empirical methods often apply very simple mathematical modelling schemes such as curve fitting methods based on experiences and post-appraisal data from previous reservoir stimulations [8]. Although these techniques provide ‘rule of thumb’ guides to the design engineer, they lack robustness in terms of honouring physical first principles and so they lack good feedback information once data trends drift from previous responses. Analytical solutions are a step in the right direction in that they offer a sound theoretical basis for the observed responses [9]. So, for example, the fracture aperture width will be a function of fluid pressure based on Sneddon’s

elasticity formulation [8]. Avoiding the introduction of any non-elastic effects means that the final equations can be readily solved without resorting to numerical techniques such as the finite difference and finite element methods. So although these techniques provide a feedback mechanism, the underlying assumptions, like elastic behavior of the rock body or steady state flow in the fracture region, might be too restrictive when dealing with a more general case such as a tight shale reservoir with numerous sets of natural fractures. The semi-analytical build on the analytical solutions by offering a numerical approach on specific parts of the governing equations. An example here would be a hybrid technique which uses an analytical solution on the fracture width versus fluid pressure relationship, but solves numerically the transient fluid flow in the fracture region [9]. Numerical methods provide the most robust schemes by allowing nonlinear behavior to be represented in both the evolution of mechanical stresses in the rock, plus the fracture fluid flow. This benefit comes at the expense of increased run-time and the necessity of an experienced numericist who understands the underlying assumptions in the model. With increasing CPU power numerical techniques such as the finite element and discrete element methods are now seen as attractive modelling approaches even when complex fracturing is one of the key mechanisms in the design process.

In broad terms the main numerical schemes appropriate for this class of problem include the FEM (Finite Element Method) [10,11,12] in its pure continuum form [13], the Discrete Fracture Network (DFN) geomechanical and continuum flow models [14], the Displacement Discontinuity Method (DDM) geomechanical and flow models [15,16,17], the combined FEM/DEM (Discrete Element Method) [18] technique plus the more recent Extended Finite Element Method (XFEM) [4,19].

The pure continuum FEM models rely on a combined coupled damage and tensile constitutive model (e.g. a unified Mohr-Coulomb with Rankine cap constitutive model) with a single porosity model to capture porous flow. The fracture propagation is captured via the volume increase through the material model, which is able to represent the pressure drops observed during fracture [13]. These models readily allow the implementation of sophisticated constitutive models and due to their simplistic form the fracture propagation does not require topology change. However, fine meshes are often required near fractured regions. Even then the fracture smears local stress fields leading to spurious values. In addition, the inclusion of a proppant transport model is difficult when undertaking a purely continuum FEM approach.

The DFN geomechanical and continuum flow models are often used within the petroleum industry [14]. They permit the use of different discretisations for the geomechanical and flow fields (e.g. finite element for the geomechanical field and finite volume for the flow field). Standard dual porosity reservoir simulators are used to capture matrix and fracture fluid flow. The hydraulic fracture process, however, strongly couples the two main governing fields and this is poorly represented by these classes of models.

The DDM uses the elastic Boundary Element Method (BEM) to capture the relationship between fracture surface pressure and the resulting aperture [15,16,17]. In these models only the fractures are discretised and this reduces the size of the problem which is an attractive benefit in 3D. Furthermore, in contrast to continuum FEM models, it is possible to capture the transport of proppant inside the propagating fracture. However, these models set restrictions on the material characterisation which are generally limited to homogenous and isotropic elastic. With these models it is difficult to accommodate complex 3D geometries and stress fields. In addition, heterogeneity is only defined via the existence of natural fractures.

The Discrete Element approach is able to mimic bond breakage, which occurs during strain softening, via a cohesive element [18,20]. It is, however, often assumed that an element edge pre-seeds the fracture direction, negating the possibility of truly complex fractures forming which are commonly observed in largely heterogeneous reservoirs.

XFEM contrasts sharply with the Discrete Element Method by using a purely continuum approach and captures crack deformation via discontinuous fields, namely the partition of unity functions [4]. The method has been coupled to fracture fluid flow models to simulate the propagation of hydraulic fractures [19]. To predict crack growth these special functions must track through the mesh and this can lead to book-keeping difficulties in complex 3D fracturing.

Kolditz and co-workers have implemented object-oriented coupled thermal-hydro-mechanical (THM) FEM techniques to investigate a range of geomechanical problems, including the flow of water and heat in fractured porous media [21,22]. The investigations are limited to pre-defined discrete fracture networks. The same author has a monograph on bench-case solutions for THM processes in fractured porous media [23].

This paper describes the governing equations and implementation of a combined FEM/DEM coupled hydro-mechanical method which is able to simulate hydraulic fracture in tight shale reservoirs. A novel approach based on new dynamically updated geometrical identities is undertaken to simulate complex fracture propagation. Section 2 describes the key governing equation, along with links to important flow concepts such as channel flow and leak-off. Section 3 develops the governing equations into a Galerkin finite element discretization. In addition, the adopted coupling scheme, namely implicit-explicit solution and communication, is presented along with a novel geometry based fracturing algorithm which includes local remeshing to avoid a computationally expensive global remesh. Section 4 describes the link between the geomechanical model and microseismicity. Finally, Section 5 presents results illustrating the numerical capability for modelling fracture propagation in both intact and naturally fractured reservoirs. In this section a validation model is also presented. The new technology ELFEN TGR (Tight Gas Reservoir) is implemented in the software package ELFEN (Rockfield Software Ltd, Swansea, UK) [24].

## 2. Governing equations

### 2.1. Overall methodology

Based on hydraulic fracture field practice, an ELFEN TGR analysis is divided into 5 key stages [24]:

1. Initiation of model effective stresses, pore pressures and fracking fluid pressures;
2. Pad hydraulic fracturing;
3. Slurry hydraulic fracturing;
4. Flowback and clean-up of the fractured region;
5. Gas production.

This paper concentrates on stages 1 and 2 with the remaining stages left for future publications. Coupling between the effective stresses in the rock matrix, pore fluid flow in the rock matrix and finally fracture fluid flow is accomplished via a staggered coupling scheme [25]. The three main sets of governing equations are [26,27]:

1. Equilibrium of the mechanical stress and pore fluid pressure of the rock formation with external loads (structure field);
2. Porous flow in the rock formation (seepage field);
3. Fluid flow in the fracture region (network field).

The main target application is the hydraulic stimulation of tight gas shale reservoirs. To fully mimic the physics for this class of problem requires a complex multi-phase flow simulator due to the interaction between the invading fracture fluid and in-situ reservoir gas. In this paper it is assumed that due to the high compressibility of the dry gas (e.g. methane) inside the shale pore space, the effective resistance of this fluid phase is insignificant when compared to the effective stresses generated in the reservoir rock. A drained response is therefore assumed during hydraulic stimulation. As a consequence of this assumption, the porous flow in the rock formation (i.e. seepage field governing equations) is only partially included in this paper when it is required in the context of equating equilibrium between the total external and internal load vectors; more details on the seepage field formulation can be found in [28].

### 2.2. Geomechanical equations

The main governing equations are derived assuming:

1. Equilibrium of stresses with an appropriate constitutive model which is able to mimic both tensile and shear failure;
2. Mass conservation of fluid flow inside the fracture region with a flow constitutive response able to recover parallel plate flow theory. This leads to the well-known cubic flow rule [29].

The update of the mechanical stresses satisfies the momentum balance equation, with the assumption that fluid acceleration relative to the solid and the convective terms can be ignored [30]. The mechanical governing equation is given by [28]:

$$\mathbf{L}^T(\boldsymbol{\sigma}' - \alpha \mathbf{m} p_s) + \rho_B \mathbf{g} = \mathbf{0} \quad (1)$$

where  $\mathbf{L}$  is the spatial differential operator,  $\boldsymbol{\sigma}'$  is the effective stress tensor,  $\alpha$  is the Biot coefficient,  $\mathbf{m}$  is the identity tensor,  $p_s$  is the pore fluid pressure in the rock formation,  $\rho_B$  is the wet bulk density and  $\mathbf{g}$  is the gravity vector.

The fracture fluid flow governing equation is given by (see Fig. 1 for schematic of link between fracture fluid flow and fracture opening) [28]:

$$\frac{\partial}{\partial x} \left[ \frac{k^{fr}}{\mu_n} (\nabla p_n - \rho_{f_n} \mathbf{g}) \right] = S^{fr} \frac{dp_n}{dt} + \alpha(\Delta \dot{e}_e) \quad (2)$$

where  $k^{fr}$  is the intrinsic permeability of the fractured region,  $\mu_n$  is the viscosity of the fracturing fluid,  $p_n$  is the fracturing fluid pressure,  $\rho_{f_n}$  is the density of the fracture fluid,  $S^{fr}$  is the storage coefficient which is effectively a measure of the compressibility of the fractured region when a fluid is present and  $\Delta \dot{e}_e$  is the aperture strain rate [26]. Assuming parallel plate theory the intrinsic permeability of a fractured region is given by [28]:

$$k^{fr} = e^2 / 12 \quad (3)$$

where  $e$  is the fracture element aperture. The storage term is given by:

$$S^{fr} = (1/e)[(1/K_n^{fr}) + (e/K_f^{fr})] \quad (4)$$

where  $K_n^{fr}$  is the fracture normal stiffness and  $K_f^{fr}$  is the bulk modulus of the fracturing fluid [28].

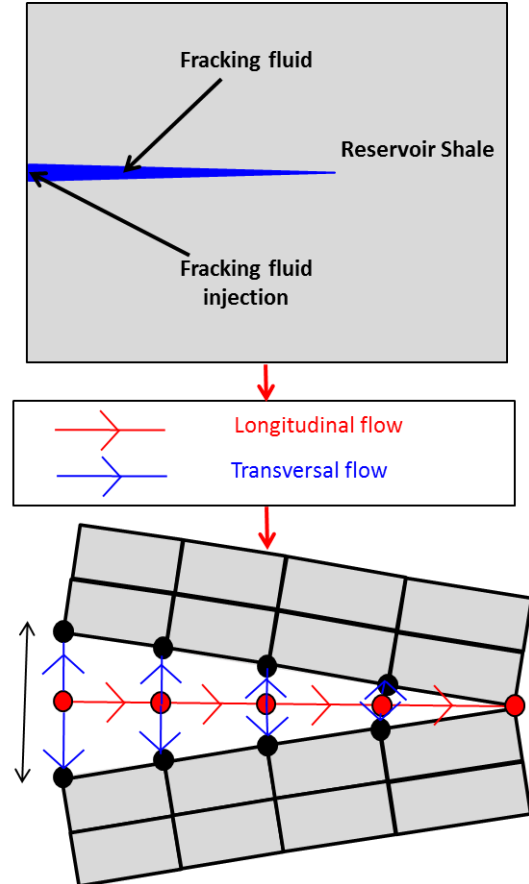


**Fig. 1 Schematic of hydraulic stimulation (top) and the modelling approach (bottom)**

### 2.3. Mechanical material model

The reservoir rock stresses are governed by three core material characteristics:

1. Elasticity;

2. Mohr-Coulomb plasticity;
3. Rankine tensile failure.

Shales are typically laminated and hence possess a preferred structure with elastic anisotropy. The Mohr-Coulomb plasticity and Rankine tensile failure constitutive models are captured using a combined single surface yield envelope as shown in Fig. 2, where  $\sigma_1$ ,  $\sigma_2$  and  $\sigma_3$  are the 3 principal stresses and  $f_{t_1}$ ,  $f_{t_2}$  and  $f_{t_3}$  are the corresponding tensile strengths [31]. In this paper it is assumed for simplicity that the shale is isotropic.

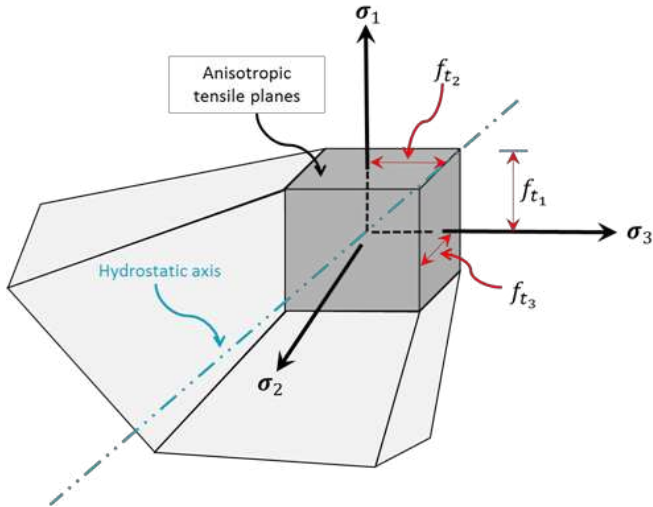


**Fig. 2 Mohr-Coulomb with Rankine tensile corner in principal stress space**

The Rankine tensile model is particularly important in hydraulic fracture modelling as the minimum principal stress at the fracture tip is tensile which allows for continued fracture propagation. The Finite Element method is a continuum-based theory and so it is subject to the well-known limitations for strain softening material models. The key shortcoming being the mechanical response is strongly mesh size dependent [32]. In a physical theory this is unacceptable therefore corrective methods have been applied to ensure mesh independent behavior, the most common approach involves including a mesh size length scale at the material level adjusting the softening slope, a process known as regularization [31].

A typical continuum extensional uniaxial stress-strain response for a quasi-brittle material is shown in Fig. 3 ( $\varepsilon_0$  and  $\varepsilon_f$  are the uniaxial yield and failure strains respectively). The pre-yield response is governed by elasticity parameters, Young's modulus  $E$  and Poisson's ratio  $\nu$ . Only two parameters are necessary to characterize the post-yield response, tensile strength  $f_t$  and fracture energy  $G_f$ . To ensure objective energy dissipation in arbitrary meshes the softening slope  $H$  is dependent on an element characteristic length  $C_l$  [31]. This approach is popular and simple to implement in finite/discrete element codes and yields global system responses that are mesh independent. Further applications of this technique can be found in the literature [33,34].

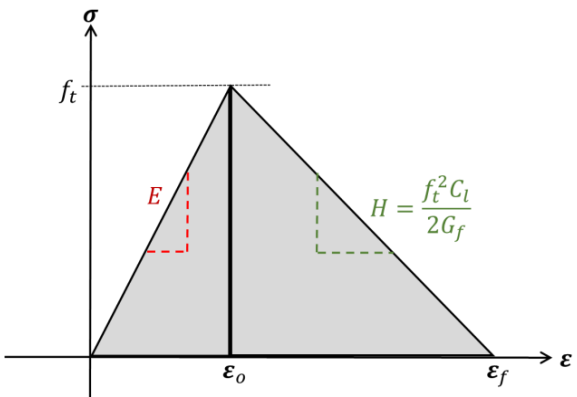


**Fig. 3 Typical uniaxial continuum damage response**

#### 2.4. Fracture fluid flow

In hydraulic fracturing of tight shales typically two fracking fluids are used, either:

1. Slickwater;
2. Cross-linked gels.

Due to the low viscosity, slickwater is often preferred to save on overall energy usage to drive the fractures. However, slickwaters are particularly poor at transporting proppant grains through the opening narrow channels. Populating the fracture with a uniform distribution of proppant is thought essential for the overall production rates of the reservoir. In contrast, viscous cross-linked gels are very good at transporting proppant grains but often do not produce the long fractures required to significantly increase the overall permeability of the fractured region. In practice hydraulic fracture pump schedules use a combination of slickwaters and cross-linked gels in sequence to ensure both a long fracture is created and subsequently proppant grains transported to the tip of the fracture, so in essence using the best qualities of both fracturing fluid types.

Macroscopically the slickwater exhibits Newtonian fluid characteristics and the crossed-linked gels non-Newtonian behaviour. In an effort to reduce the viscosity at higher strain rates, a shear-thinning cross-linked gel is commonly adopted. Constitutively, this behavior can be captured using the non-Newtonian Power Law model:

$$\tau = K\gamma^n \quad (5)$$

where  $\tau$  is the fluid shear stress,  $\gamma$  is the fluid shear strain rate,  $K$  is the consistency index and  $n$  is the power law exponent. For the simulation of fluid flow within the fractures, the following assumptions are applied [29]:

1. The fluid is incompressible;
2. The flow is locally equivalent to the flow between two smooth, parallel plates;
3. The flow is laminar with a low Reynolds number.

#### 2.5. Fracture fluid leak-off

The petroleum industry commonly finds that approximately 50-80% of injected fluid is lost during typical hydraulic stimulation of a tight gas shale reservoir [35]. The exact cause of this loss is not known but some hypotheses include the migration of fracturing fluid into fissures adjacent to the main propagating fracture and capillary action due to the

inherent small pore throat radii of the shale grains. Whatever the root cause one effect of this fluid loss is a drop in fracture fluid pressure as the fracture propagates, so mimicking this behavior is extremely important in order to capture the correct fracture volume and length generated during stimulation. This behavior is represented using a 1D Carter leak-off model (transversal flow) which has an in-built decay of leak-off rate due to the assumed formation of a filter cake on the exposed fracture surface over time [5]. The model assumes an initial volume loss  $V_{sp}$  per unit area over a spurt time  $t_{sp}$  followed by a constant leak-off coefficient  $C$  as:

$$t - t_{exp} < t_{sp}; \quad q_l = \frac{V_{sp}}{t_{sp}} \quad (6)$$

$$t - t_{exp} \geq t_{sp}; \quad q_l = \frac{C}{\sqrt{t - t_{exp}}}$$

where  $t$  is the current model time,  $t_{exp}$  is the time at which a fracture surface is exposed for leak-off and  $q_l$  is the 1D normal leak-off velocity. The spurt volume is determined from fluid loss experiments (see Fig. 4, [36]). In addition, Fig. 4 shows the controlling leak-off mechanisms as they evolve through the experiment. Initially, the flow characteristics of the reservoir (e.g. the reservoir fluid viscosity or its intrinsic permeability) are dominant in controlling the degree of fluid leak-off which invades the host rock. However, once a filter cake has formed on the exposed fracture surface, this controls the fluid loss and the rate reduces, eventually tending to a steady state fluid loss.

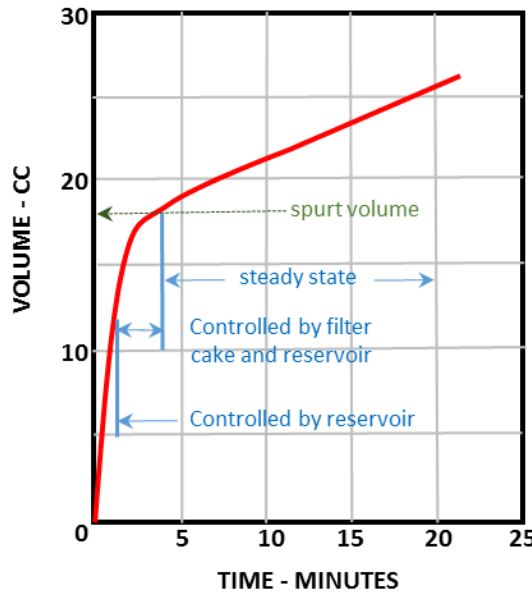


Fig. 4 A typical dynamic fluid loss experiment

The 1D Carter leak-off model in Eq. (6) is independent of the pressure difference between the fracture fluid pressure and the rock formation pore fluid pressure. More sophisticated leak-off models which are functions of the pressure difference can be found in the literature [24] but will not be discussed further here.

A single phase analysis is assumed between fluids in both the fracture and porous media regions. In practice this

states that the fracturing fluid and the tight reservoir gas cannot mix. A special treatment is invoked which allows the fluid to be extracted from the fracture and stored in a separate storage block (i.e. fluid is not transferred into the rock formation). The extraction of fluid mass is important as this is a key driver in the final hydraulic fracture length with lengths significantly reduced for those fractures experiencing high degrees of leak-off. During the flowback stage the stored fluid is available for extraction so mass conservation of the fracturing fluid in the global system is maintained.

### 3. Numerical algorithms

#### 3.1. Overall methodology

Two solutions are used to update the main governing equations:

1. For the evolution of the mechanical stresses an explicit solution method is used. This method is most advantageous when dealing with material strain softening where implicit schemes can struggle to attain convergence during the material stress update;
2. For evolution of fracture fluid pressure an implicit solution method is adopted. As the fracture flow region is limited to a small part of the problem domain the computational overhead is low. In addition, the convergence rates are robust for a wide range of fluid properties and fracture aperture widths.

#### 3.2. Discretised geomechanical equations

The two governing equations for the mechanical (structure field) and fracture fluid flow (network field) are semi-discretised using the finite element method. It is assumed that the shape functions can be independent for structure  $\mathbf{N}_u$ , seepage  $\mathbf{N}_s$  and network  $\mathbf{N}_n$  fields, respectively.

$$\mathbf{B}_u = \mathbf{L}_u \mathbf{N}_u, \mathbf{B}_s = \mathbf{L}_s \mathbf{N}_s \text{ and } \mathbf{B}_n = \mathbf{L}_n \mathbf{N}_n \quad (7)$$

where  $\mathbf{L}_u$ ,  $\mathbf{L}_s$  and  $\mathbf{L}_n$  are the gradient operators for the structure, seepage and network fields respectively and finally  $\mathbf{B}_u$ ,  $\mathbf{B}_s$  and  $\mathbf{B}_n$  are the shape function spatial gradient matrices for the structure, seepage and network fields respectively. It should be noted that the seepage field component is only included to satisfy completeness of the equilibrium equation which is a function of the total and not effective stress tensor. The finite element discretized structure field equation is given by:

$$\int_{\Omega_u} \mathbf{B}_u^T \boldsymbol{\sigma}' \partial \Omega_u - \int_{\Omega_s} \mathbf{B}_u^T \alpha \mathbf{m} \mathbf{N}_s \partial \Omega_s p_s = \mathbf{f}_u \quad (8)$$

where  $\Omega_u$  is the structure domain,  $\Omega_s$  is the seepage domain and  $\mathbf{f}_u$  is the mechanical load vector. The effective stress tensor  $\boldsymbol{\sigma}'$  is computed using the combined Mohr-Coulomb and Rankine cap material model. The finite element discretized network field equation is given by:

$$\int_{\Omega_n} \mathbf{B}_n^T \frac{k^{fr}}{\mu_n} \mathbf{B}_n p_n \partial \Omega_n + \int_{\Omega_n} \mathbf{N}_n^T S^{fr} \mathbf{N}_n \partial \Omega_n \frac{\partial p_n}{\partial t} = \mathbf{f}_n \quad (9)$$

where  $\Omega_n$  is the network domain and  $\mathbf{f}_n$  is the fracture fluid flow load vector. The structure and network fields coupled governing equations can be written in matrix form as:

$$\begin{bmatrix} \mathbf{M} & \mathbf{0} \\ \mathbf{0} & \mathbf{0} \end{bmatrix} \begin{bmatrix} \dot{\mathbf{u}} \\ \dot{p}_n \end{bmatrix} + \begin{bmatrix} \mathbf{0} & \mathbf{0} \\ \mathbf{Q}_n^T & \mathbf{S}_n \end{bmatrix} \begin{bmatrix} \dot{\mathbf{u}} \\ \dot{p}_n \end{bmatrix} + \begin{bmatrix} \mathbf{K} & \mathbf{0} \\ \mathbf{0} & \mathbf{H}_n \end{bmatrix} \begin{bmatrix} \mathbf{u} \\ p_n \end{bmatrix} = \begin{bmatrix} \mathbf{f}_u \\ \mathbf{f}_n \end{bmatrix} \quad (10)$$

with matrices and vectors defined as:

$$\begin{aligned} \mathbf{M} &= \int_{\Omega_u} (\mathbf{N}_u)^T \rho_B \mathbf{N}_u \partial \Omega_u \\ \mathbf{K} &= \int_{\Omega_u} (\nabla \mathbf{N}_u)^T D \nabla \mathbf{N}_u \partial \Omega_u \\ \mathbf{Q}_n &= \int_{\Omega_n} (\nabla \mathbf{N}_u)^T \mathbf{m} \mathbf{N}_n \partial \Omega_n \\ \mathbf{S}_n &= \int_{\Omega_n} (\mathbf{N}_n)^T S^{fr} \mathbf{N}_n \partial \Omega_n \\ \mathbf{H}_n &= \int_{\Omega_n} (\mathbf{N}_n)^T \frac{e^2}{12\mu_n} \nabla \mathbf{N}_n \partial \Omega_n \\ \mathbf{f}_u &= \int_{\Omega_u} (\mathbf{N}_u)^T \rho_B \mathbf{b} \partial \Omega_u + \int_{\Omega_u} (\mathbf{N}_u)^T t \Gamma_u \\ \mathbf{f}_n &= - \int_{\Omega_n} (\mathbf{N}_n)^T \nabla^T \left( \frac{e^2}{12\mu_n} \rho_{f_n} \mathbf{b} \right) \partial \Omega_n \\ &\quad + \int_{\Omega_n} (\mathbf{N}_n)^T q \Gamma_n \end{aligned} \quad (11)$$

where  $D$  is the material stiffness matrix,  $\Gamma_u$  and  $\Gamma_n$  are the boundary regions of the structure and network fields respectively,  $t$  is the external traction load which in the present context is the fluid pressure along the exposed fracture surface and  $q$  is the fracturing fluid flux. This sink term is used in conjunction with the 1D leak-off when fracturing fluid loss is a significant part of the analysis.

### 3.3. Coupling strategy: an overview

A staggered coupling scheme is adopted in which the mechanical governing equation is solved explicitly [11] and the fracture fluid flow governing equation is solved implicitly [25,26,30,37,38,39,40]. This implies that in practice there are many more explicit time steps per implicit time step and hence on the mechanical field the fracture fluid pressure needs to be updated using intermediate values between coupling times. The coupling between structure, seepage and network fields is shown in Fig. 5.

The motion of the fracture aperture is computed in the structure field and this information is transferred to the network field to update the permeability characteristics of the propagating fracture. Likewise, the fracturing fluid pressure is computed in the network field and this is transferred to the structure field where it acts as an external traction load on the fracture surface. In this paper the structure and seepage fields are considered uncoupled.

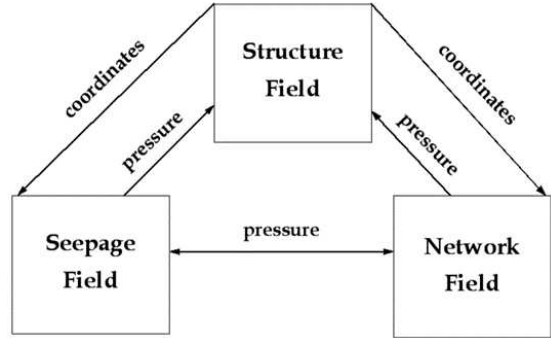


**Fig. 5 Coupling between structure, seepage and network fields**

A key feature in the proposed formulation is the treatment of the network fluid pressure in both structure and network fields. Both fields compute locally their own network fluid pressure and coupling is maintained via a predictor-corrector scheme as outlined in Section 3.6.

Since this class of problem investigates tight gas shale reservoir with isotropic Young's moduli in the range of 30-60 GPa [41], the time steps could be quite small unless remedial measures are undertaken. Mass scaling techniques [42] are performed on relevant parts of the finite element mesh whenever an explicit time step is liable to drop below a threshold value. These are typically near the fracture tip with a maximum scaling factor of 100. Global system kinetic and strain energies are performed to ensure a quasi-static solution is attained.

### 3.4. Coupling strategy: communication scheme

Fig. 6 shows a graphical representation of the network pressure update in both structure and network fields.

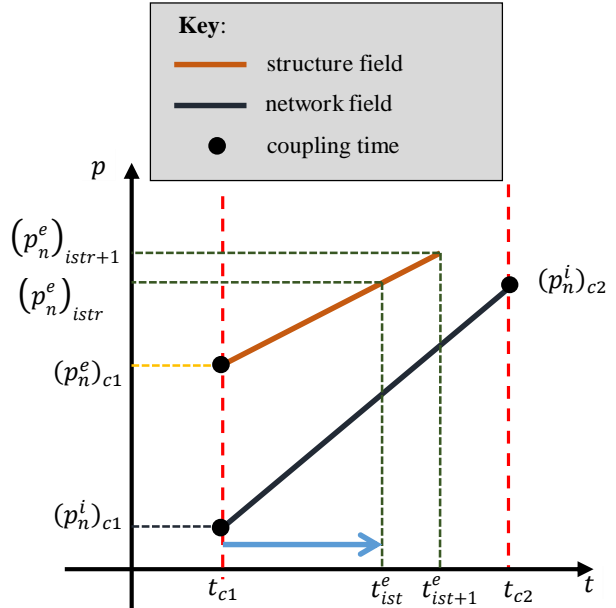


**Fig. 6 Graphical representation of fluid pressure update in both structure and network fields between successive coupling times  $t_{c1}$  and  $t_{c2}$**

A note on the notation, the superscripts  $i$  and  $e$  refer to the implicit and explicit solvers respectively. The fluid pressures

at a coupling time are usually not equal in structure and network fields, i.e.  $(p_n^e)_{c1} \neq (p_n^i)_{c1}$ . The implicit network field analysis first marches forward in time between coupling times  $t_{c1}$  and  $t_{c2}$  yielding fluid pressures  $(p_n^i)_{c1}$  and  $(p_n^i)_{c2}$ .

Fig. 7 presents the communication between implicit and explicit solvers which takes place across successive coupling times  $t_{c1}$  and  $t_{c2}$ . More details regarding the individual implicit and explicit solution updates can be found in Sections 3.5 and 3.6 respectively

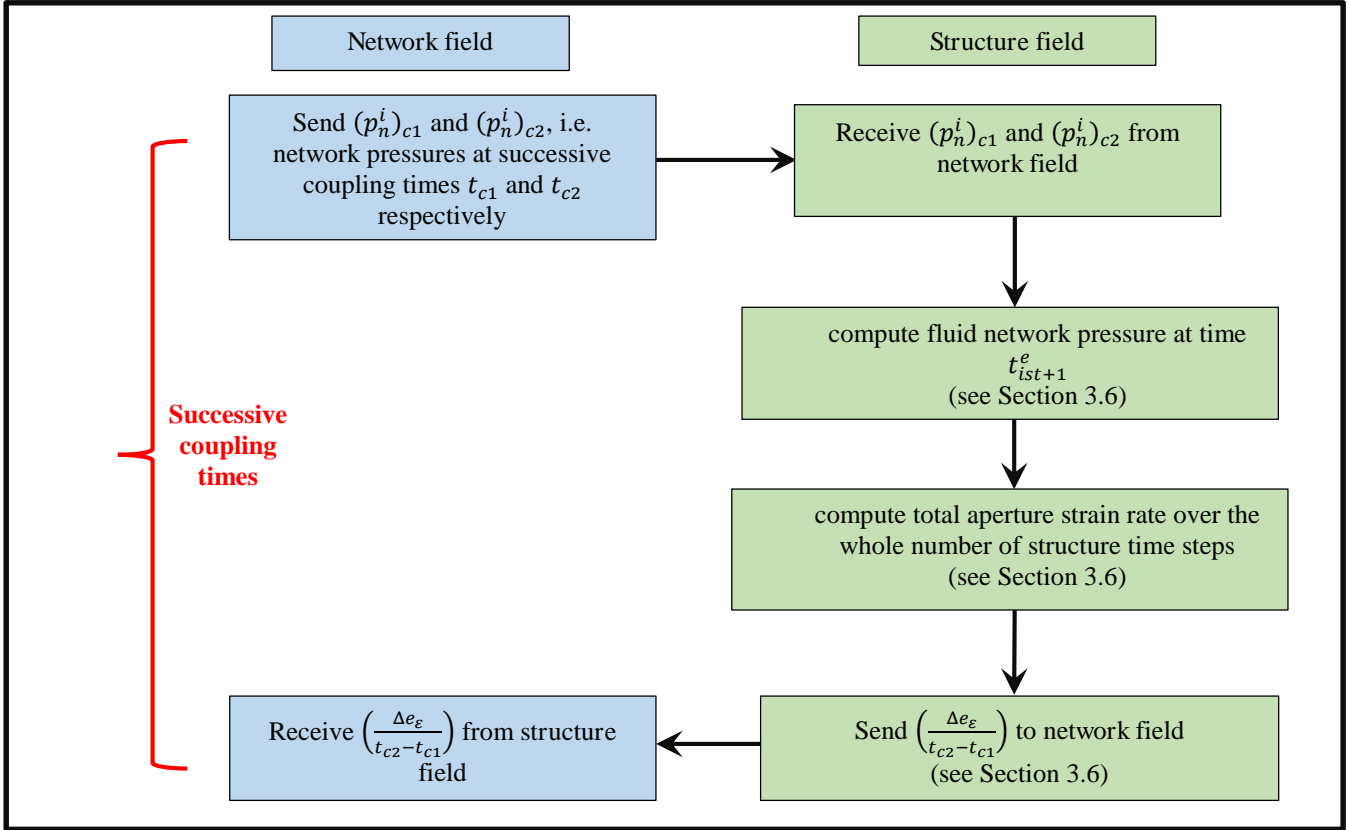


**Fig. 7** Communication between network and structure fields during successive coupling times

### 3.5. Time integration: network field implicit solution

From Eq. (10) the network field at the current time  $t_{k+1}$  can be written as (where the subscript  $k + 1$  implies that the corresponding matrix or vector term is computed at the current time):

$$\begin{aligned} (\mathbf{Q}_n^T)_{k+1}(\dot{\mathbf{u}})_{k+1} \\ + (\mathbf{S}_n)_{k+1}(\dot{p}_n)_{k+1} + (\mathbf{H}_n)_{k+1}(p_n)_{k+1} \\ = (\mathbf{f}_n)_{k+1} \end{aligned} \quad (12)$$

A generalized Newmark procedure GN11 is performed to update the nodal network pressure  $p_n$  between successive time steps  $t_k$  and  $t_{k+1}$ :

$$(p_n)_{k+1} = (p_n)_k + (p_n)_k \Delta t_{imp} + \beta_0 \Delta \dot{p}_n \Delta t_{imp} \quad (13)$$

$$(\dot{p}_n)_{k+1} = (\dot{p}_n)_k + \beta_1 \Delta \dot{p}_n \quad (14)$$

where  $\Delta t_{imp} = t_{k+1} - t_k$  is the implicit solution time increment. In addition  $\beta_0$  and  $\beta_1$  are the integration parameters set as  $\beta_0 = 0$  and  $\beta_1 = 1.0$ . Eq. (12) can be rewritten as:

$$\begin{aligned} \boldsymbol{\psi}_{k+1}^{itn} = (\mathbf{f}_n)_{k+1}^{itn} - (\mathbf{S}_n)_{k+1}^{itn}(\dot{p}_n)_{k+1}^{itn} \\ - (\mathbf{H}_n)_{k+1}^{itn}(p_n)_{k+1}^{itn} \\ - (\mathbf{Q}_n^T)_{k+1}^{itn}(\dot{\mathbf{u}})_{k+1}^{itn} = \mathbf{0} \end{aligned} \quad (15)$$

where the superscript  $itn$  refers to the iteration number. Clearly, convergence is achieved when  $\boldsymbol{\psi}_{k+1}^{itn} \rightarrow \mathbf{0}$ . The unknown parameter in Eq. (15) is  $\Delta \dot{p}_n$  and this is computed using the Newton-Raphson method:

$$-\frac{\partial \boldsymbol{\psi}_{k+1}^{itn}}{\partial \Delta \dot{p}_n} d(\Delta \dot{p}_n)^{itn} = \boldsymbol{\psi}_{k+1}^{itn} \quad (16)$$

Linearisation of Eq. (15) leads to the final transient equation that is then used to update the nodal network pressures:

$$\begin{aligned} [\beta_1(\mathbf{S}_n)_{k+1}^{itn} + \beta_0 \Delta t (\mathbf{H}_n)_{k+1}^{itn}] d(\Delta \dot{p}_n_n)^{itn} \\ = (\mathbf{f}_n)_{k+1}^{itn} - (\mathbf{S}_n)_{k+1}^{itn}(\dot{p}_n)_{k+1}^{itn} \\ - (\mathbf{H}_n)_{k+1}^{itn}(p_n)_{k+1}^{itn} \\ - (\mathbf{Q}_n^T)_{k+1}^{itn}(\dot{\mathbf{u}})_{k+1}^{itn} \end{aligned} \quad (17)$$

Once  $\Delta \dot{p}_n$  is equated then the fluid pressure terms in Eq. (13) and (14) are updated to the current problem time  $t_{k+1}$ . In the present formulation the implicit solution initially advances ahead of the explicit solution of the structure field and during this stage the aperture and aperture strain rate terms are assumed constant over a single implicit solution time increment. This implies that the storativity and permeability matrix terms are also constant.

### 3.6. Time integration: structure field explicit solution

Time integration of the structure field adopts the standard central difference scheme to update the nodal accelerations, velocities and displacements [10,31].

Since in practice compared with the implicit solution scheme the explicit solution requires many more time integration steps it is necessary to update the network field fluid pressure at intermediate steps between coupling times ( $t_{c1}$  and  $t_{c2}$  respectively, see Fig. 6). The following presentation builds on the parameters shown in Fig. 6 and they are defined in more detail here. As the implicit network field advances ahead of the explicit structure field then from the perspective of the structure field the network fluid pressures ( $p_n^i$ )<sub>c1</sub> and ( $p_n^i$ )<sub>c2</sub> at successive coupling times  $t_{c1}$  and  $t_{c2}$  are known values. The structure field network fluid pressures ( $p_n^e$ )<sub>c1</sub> are also known at the start of the coupling interval  $t_{c1}$ . The goal is to compute the network fluid pressure between coupling times on the explicit structure field using only these values. It is assumed that this value can be decomposed into 3 components as:

$$(p_n^e)_{istr+1} = (p_n^i)_{int} + \Delta p_s + \Delta p_d \quad (18)$$

where ( $p_n^e$ )<sub>istr+1</sub> is the network fluid pressure at the intermediate step  $istr + 1$  between coupling times  $t_{c1}$  and  $t_{c2}$ . The number of intermediate steps is dependent on the ratio of the explicit time step size to the coupling time interval. ( $p_n^i$ )<sub>int</sub> is the linearly interpolated network pressure from the implicit values at time  $t_{istr+1}^e$ :

$$(p_n^i)_{int} = (p_n^i)_{c1} + \frac{t_{istr+1}^e - t_{c1}}{t_{c2} - t_{c1}} ((p_n^i)_{c2} - (p_n^i)_{c1}) \quad (19)$$

The incremental change in network fluid pressure due to the storativity and aperture change is given by:

$$\Delta p_s = -(1/S^{fr}) \Delta e_\varepsilon \quad (20)$$

Where  $\Delta e_\varepsilon$  is the change in aperture strain computed between successive explicit time steps  $istr$  and  $istr + 1$  as:

$$\Delta e_\varepsilon = \frac{e_{istr+1} - e_{istr}}{0.5(e_{istr+1} + e_{istr})} \quad (21)$$

Where  $e_{istr+1}$  and  $e_{istr}$  are the apertures extracted at times  $t_{istr+1}^e$  and  $t_{istr}^e$  respectively. The third component is a measure of the difference between the implicit and explicit computed network pressures at the start of a coupling interval. This difference is linearly ramped off over the coupling interval:

$$\Delta p_d = \frac{t_{c2} - t_{istr+1}^e}{t_{c2} - t_{c1}} ((p_n^i)_{c1} - (p_n^e)_{c1}) \quad (22)$$

The coupling interval must be appropriately set; if it is not tight enough there will be an unacceptable drift between the two values and, conversely, too tight a coupling interval can lead to increased run-time without improved accuracy of the solution.

### 3.7. Time integration: coupling parameters

The present formulation exhibits good convergence

properties with the implicit solution scheme typically converging within a few iterations. For hydraulic fracture design cases pumping times are usually measured in the order of thousands of seconds and through investigation it has been found that a coupling interval of 1.0s is typically appropriate for this class of problem.

### 3.8. Geometry based fracture prediction

The geometry insertion technique is a means of introducing new geometry lines (in 2D hydraulic stimulation models) into the finite element discretization which do not necessarily follow the edges of the finite element mesh. The newly introduced geometry lines simulate fracture growth during hydraulic stimulation. In addition, a local remesh algorithm is implemented which only operates around the fracture tip region, thus avoiding the need for a computationally exhaustive global remesh.

At the material level each element response follows continuum damage theory (see Section 2.3) and the key constitutive parameters like stress, strain and damage are spatially located at the element Gauss point. The damage indicates the degree of softening which an element has undergone during loading, with a value of 0 indicative of no damage and 1 indicative of fully damaged. In term of the physical response this represents the coalescence of micro-flaws leading to the creation of two new fracture surfaces.

A typical fracture propagation model is shown in Fig. 8(a)-(c) with the fracture length almost doubling in size during fluid injection. The propagating fracture is not pre-seeded due to model constraints and it is freely able to follow the stress state as dictated by the model (refer to Fig. 8(b)-(c)).

A schematic of the damage process zone and its numerical treatment is shown in Fig. 9(a)-(c). This shows the opening of a crack mouth with a tensile damage zone ahead of the fracture tip. The elements in red signify that the element is fully damaged with the remaining elements below this threshold and still capable of supporting load (refer to Fig. 9(a)). The predicted fracture surface is not forced to follow the element edges and can follow the stress state as dictated by the simulation (see Fig. 9(b)). Due to the mode-1 assumption of failure, the failure direction is defined as orthogonal to the maximum tensile principal stress. When the failure path exceeds a user-specified length all points along the path are used to form a geometric entity and this finally leads to the fracture surface (Fig. 9(b)-(c)). The fracture prediction algorithm is shown in Table 1:

For each fracture tip:

- Extract material state for elements within patched region (see Fig. 10(a)-(b))
- Interpolate damage variable to element nodes (see Fig. 10(c)).
- For those nodes which have surpassed the damage threshold of 1.0 as set by the material model, construct a best-fit linear line from fracture tip through damaged nodes (see Fig. 10(d))
- If line length matches that specified by the user then the line is marked ready for fracture insertion

**Table 1 Fracture prediction**

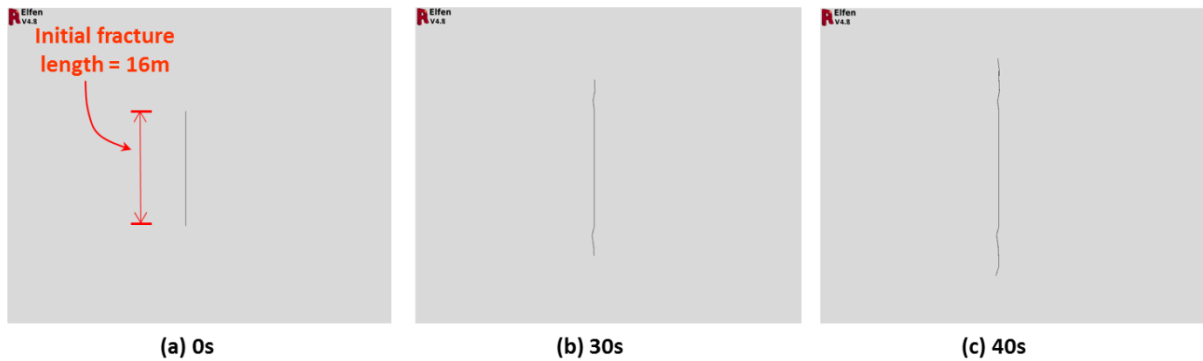


**Fig. 8(a)-(c) Evolving discrete fracture**

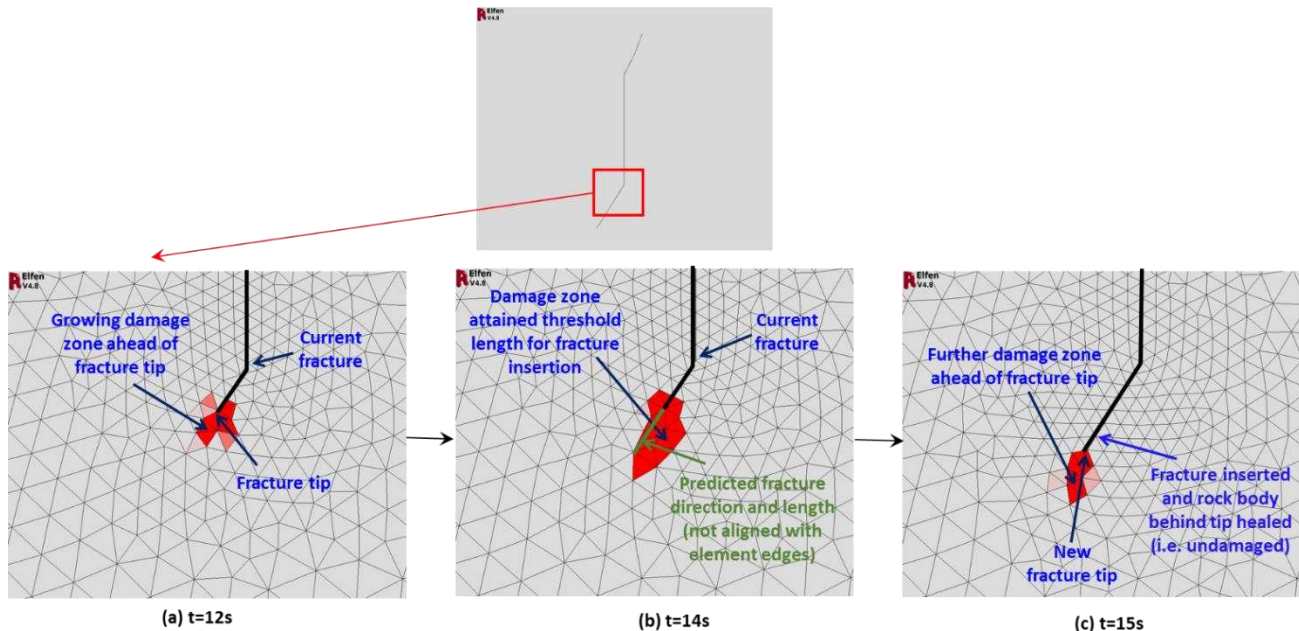


**Fig. 9(a)-(c) Fracture prediction and insertion**

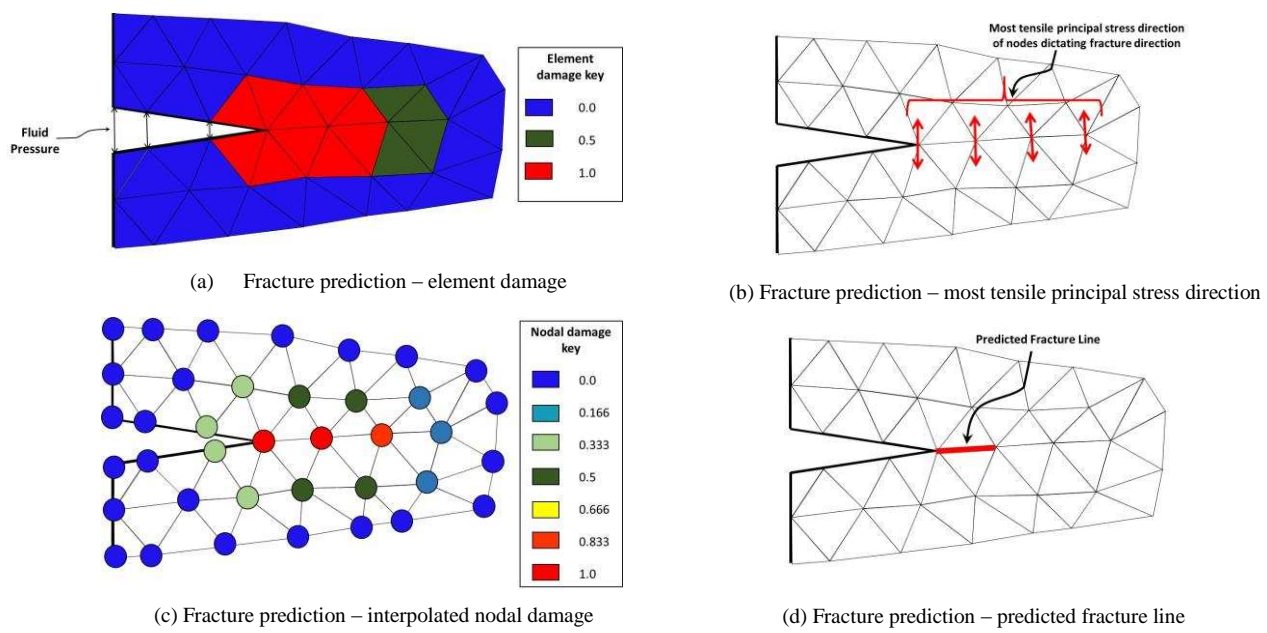


**Fig. 10(a)-(d) Predicting fracture length and direction**

### 3.9. Local remeshing around fracture tip

A very important modelling aspect is the capability to deal with meshing the new geometry in a computationally attractive manner. A local meshing methodology is employed which makes redundant the need for a traditionally expensive global remesh, which is also likely to introduce dispersion of key material variables such as stress, strain and damage indicators. The local meshing zone is defined via a patch region which is adjacent to the fracture tip and it is always very small compared to the problem size, so in relative terms the computational cost is low (refer to Fig. 11(a)).

It is very important that the remesh is only performed locally at a fracture tip. For example, in a typical industrial scale mesh of many 100,000's elements typically only a 100 elements are remeshed. The mesh in all other regions of the problem domain remains unchanged (refer to Fig. 11(b)). Clearly, fracturing is a very dynamic process in that the model is constantly changing so this procedure of following the fracture tip via a patch region and subsequently only remeshing locally is continually being updated during hydraulic stimulation. This is extremely important for this class of problem as it has been observed that for some tight gas shales stimulated fracture lengths reach values of many hundreds of meters [43].

There is a parent-child relationship between the network and fracture surface nodes which allows, for example, the fluid pressure from the network field to be transferred as an external load to a corresponding node on the fracture surface of the structure field. During a local remesh around a fracture tip this mesh topology must be maintained and this is achieved by initially stitching the mesh back to a non-discrete body, performing the local remesh on the resulting bonded domain and then displacing the elements back to their original spatial location after the remesh. This is achieved by monitoring the displacements of the fracture surfaces such that they can be returned to their position after the remesh. Since Mode I failure rather than shear failure mechanisms is considered in the present application, typically there is very little relative slip between opposing fracture surfaces during hydraulic stimulation.

Key nodal and element variables, such as displacements and stresses, are mapped between old and new meshes using standard mapping techniques (see [44] for more details). Mapping of the displacements is very important to ensure that the correct aperture is maintained after a remesh since the implicit solution network element permeability is a function of the current aperture. The newly inserted network elements are initialised to the initial reservoir fluid pressure and the increased fluid pressure from further fluid injection typically results in additional fracture opening.

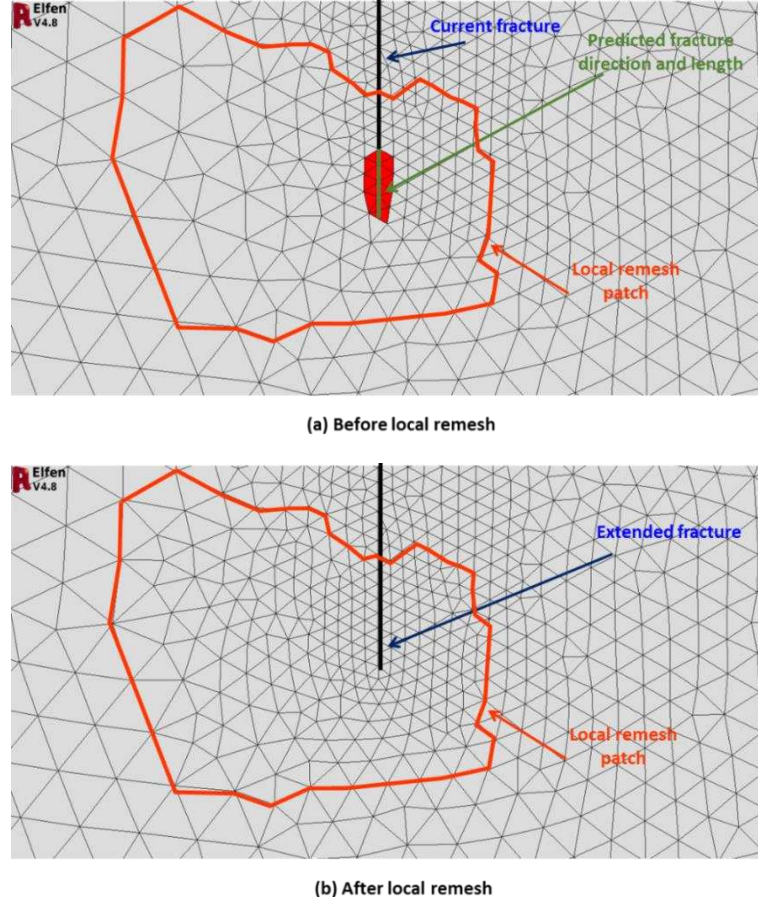


**Fig. 11(a)-(b) Local remeshing around fracture tip**

## 4. Geomechanics and Microseismicity

### 4.1. Overall methodology

The concept behind integrating geomechanics and microseismic prediction for the finite element method [45] is based on the approach described in [46]. The integrated geomechanics and microseismic prediction was applied to a North Sea field, where subsidence prediction was used to calibrate the coupled flow-geomechanical model of the field [47]. The paper was interested in monitoring high shear stress regions in the reservoir layer with the potential increased risk of microseismicity.

### 4.2. Implementation

The approach followed in this paper is outlined in the paper by Angus et al. [45]. Seismic events are monitored in space and time, where a microseismic event is predicted to occur within an element when the effective stress satisfies the Mohr-Coulomb yield envelope. Based on the differential stress tensor Angus calculates a pseudo-scalar seismic moment (i.e. stress drop) which can be used to infer microseismicity. Future work will include a method outlined by Lisjak [20] for transferring the material strain energy into a seismic energy signal for mode-1 type failure.

## 5. Numerical Examples

### 5.1. Validation model

To ensure the validity of the proposed formulation the software is compared against a well-known analytical solution in the hydraulic fracture mechanics literature. The KGD (Khristianovitch and Zheltov, Geertsma and De-Klerk) analytical solution assumes:

1. The relationship between crack or fracture surface pressure and fracture aperture is given by Sneddon's formulation
2. Steady state fluid flow inside the fracture

The implementation proposed in this paper assumes transient flow so it is only possible to partially capture the assumptions in the analytical solution. A further validation comparison is presented via a semi-analytical solution in which the mechanical response of the fracture width is once again dictated by Sneddon's equation but the flow part is solved via a 1D numerical solution using a finite difference scheme, allowing the transient effects to be captured. From Sneddon's equation, the width as a function of net pressure and fracture length is given by [1]:

$$W \propto 4 \frac{(1 - \nu^2)}{E} LP \quad (23)$$

where  $W$  is the maximum fracture width or aperture,  $E$  is the isotropic Young's modulus,  $\nu$  is the Poisson's ratio,  $L$  is the fracture length and  $P$  is the net pressure along the fracture. Assuming parallel plate flow theory for 1D laminar flow the relationship between fluid velocity and flow rate is given by:

$$\frac{dp}{dx} \propto -\frac{12Q\mu}{HW^3} \quad (24)$$

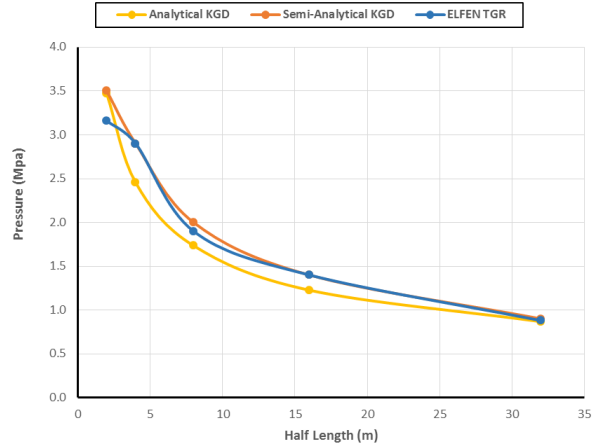
where  $p$  is the fluid pressure,  $x$  is the 1D spatial dimension,  $Q$  is the fluid injected flow rate,  $\mu$  is the fluid viscosity and  $H$  is the height of the fracture. Substituting Eq. (23) into Eq. (24) and solving the resulting ordinary differential equation via a simple separation of variables leads to the following solutions:

$$p_{sol} = \left( \frac{6Q\mu E^3}{8H^4(1 - \nu^2)^3} \right)^{0.25} L^{0.25} \quad (25)$$

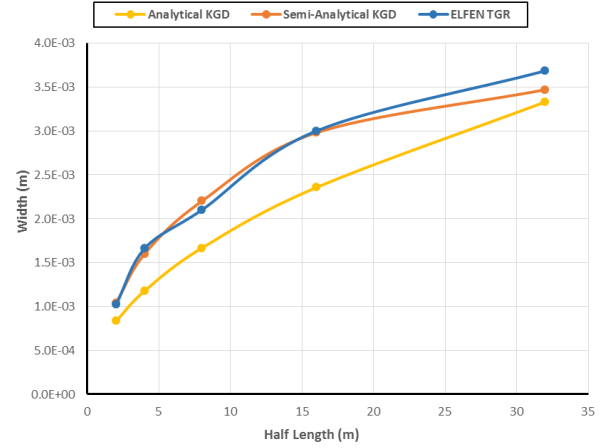
$$W_{sol} = \left( \frac{96Q\mu(1 - \nu^2)}{E} \right)^{0.25} L^{0.25} \quad (26)$$

Where  $p_{sol}$  and  $W_{sol}$  are known as the pressure solution and width solution respectively.

Fig. 12(a)-(b) shows the comparison between the software and both KGD analytical and semi-analytical solutions. It can be seen that the trends for both 'pressure versus fracture half-length' and 'fracture width versus fracture half-length' are captured with the semi-analytical KGD solution providing a better match due to its capability to mimic transient flow inside the fracture. Sneddon's solution assumes elastic behaviour so in the numerical solution fluid was only injected prior to inelastic deformation at the fracture tip.



(a) Pressure (MPa) v. half length (m)



(b) Width (m) v. half length (m)

Fig. 12(a)-(b) Comparison of software against KGD solution (analytical and semi-analytical solutions)

## 5.2. Demonstration models

The demonstration cases investigate hydraulic fracturing in both intact (see Fig. 13(a)) and naturally fractured (see Fig. 13(b)) shale reservoirs. The reservoir is modelled in plan view as a 2D plane strain domain. Hence, the model is simulating horizontal fracturing with an assumed constant extruded height or reservoir layer thickness. The outer boundaries of the model are fixed. The natural fractures are modelled with Mohr-Coulomb stick-slip contact regions [48,49]. The pre-production stresses and pore pressures are specified in Table 2. The initial stresses are not aligned with the global axis but are rotated clockwise by 40° relative to north (i.e. positive y-axis). This is indicative of the case where the horizontal wellbore is not drilled exactly parallel with the minimum principal stress.

Pre-production parameter	Value
Minimum horizontal effective stress	10 MPa
Maximum horizontal effective stress	15 MPa
Overburden effective stress	20 MPa
Reservoir pore pressure	30 MPa

**Table 2 Pre-production stresses and pore pressure  
(assumed uniform)**

The natural fractures in Fig. 13(b) are specified via a statistical variation of 4 key discrete fracture network (DFN) parameters; these are:

- Orientation (relative to north, i.e. y-axis);
- Fracture spacing;
- Fracture length;
- Persistence.

For the naturally fractured case, two DFN sets are specified with DFN parameters as stated in Table 3 and Table 4 respectively.

DFN parameter	Value
Orientation	90°
Fracture spacing	80 m
Fracture length	40 m
Persistence	80 m

**Table 3 DFN set 1**

DFN parameter	Value
Orientation	330°
Fracture spacing	30 m
Fracture length	40 m
Persistence	50 m

**Table 4 DFN set 2**

In reality the natural fractures are not perfectly aligned according to a uniform DFN parameter value and so a small standard deviation is applied to each parameter to give a small variation about the input mean (see Fig. 13(b)).

## 5.3. Mechanical and fracture fluid properties

Isotropic elasticity is assumed for the shale rock with the material parameters given in Table 5. The fracture mechanics material parameters and fracking fluid properties are stated in Table 6 and Table 7 respectively.

Material parameter	Value
Young's modulus	32,000 MPa
Poisson's ratio	0.2

**Table 5 Shale elastic properties**

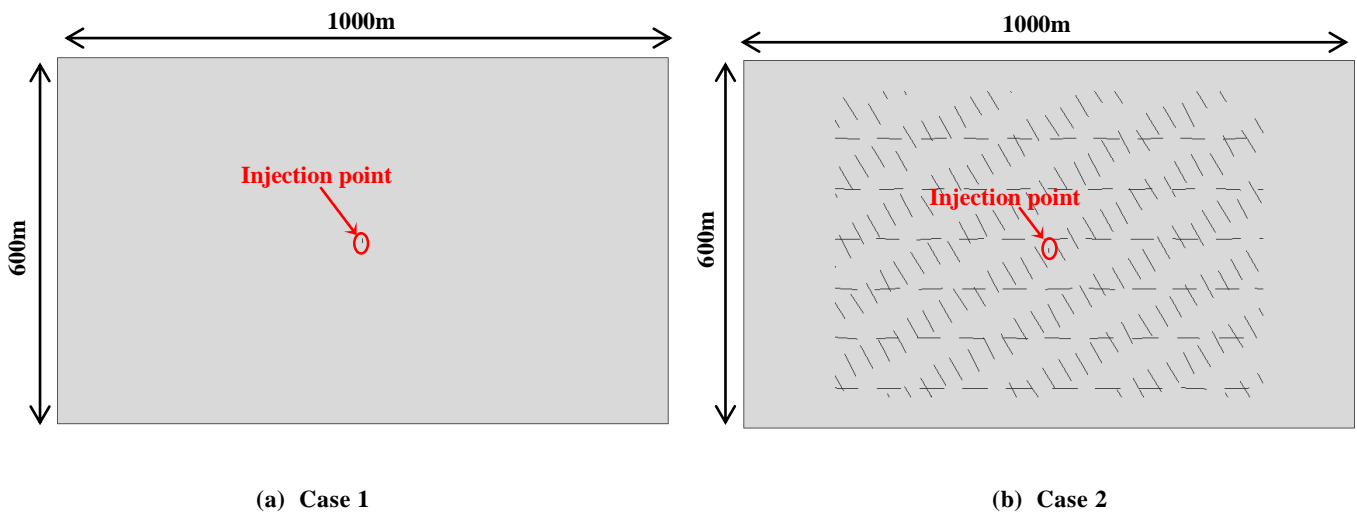


**Fig. 13(a)-(b): Case 1 - Model geometry of intact reservoir (plan view); Model geometry of naturally fractured reservoir with two DF sets (plan view)**

Material parameter	Value
Tensile strength	1.0 MPa
Fracture energy	50 N.m

Table 6 Shale fracture mechanics properties

Fluid property	Value
Viscosity	1.67E-3 Pa.s
Bulk fluid modulus	2,000 MPa

Table 7 Fracturing fluid properties

#### 5.4. Case 1: Hydraulic stimulation of intact rock

An intact shale of uniform layer thickness 10m is pumped with a slickwater fracturing fluid along with a pumping schedule as outlined in Table 8. It is assumed that the fluid loss from the fracture into the reservoir is very low.

Flow rate (m <sup>3</sup> /s)	Volume (m <sup>3</sup> )	Duration (s)
0.125	75	600

Table 8 Pumping schedule

Fig. 14 shows the orientation of the initial minimum and maximum effective horizontal principal stresses. Fig. 15(a)-(c) shows the evolution of the propagating fracture. In particular, it can be observed that the fracture propagates towards the maximum compressive stress and maintains this direction throughout the fluid injection phase. In practice

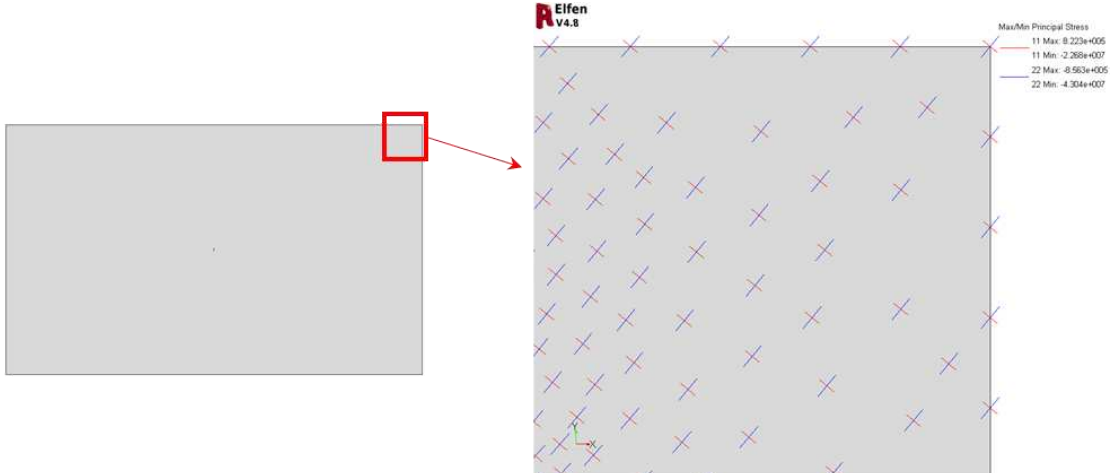


Fig. 14 Case 1: Pre-production minimum and maximum principal directions (red – minimum; blue – maximum)

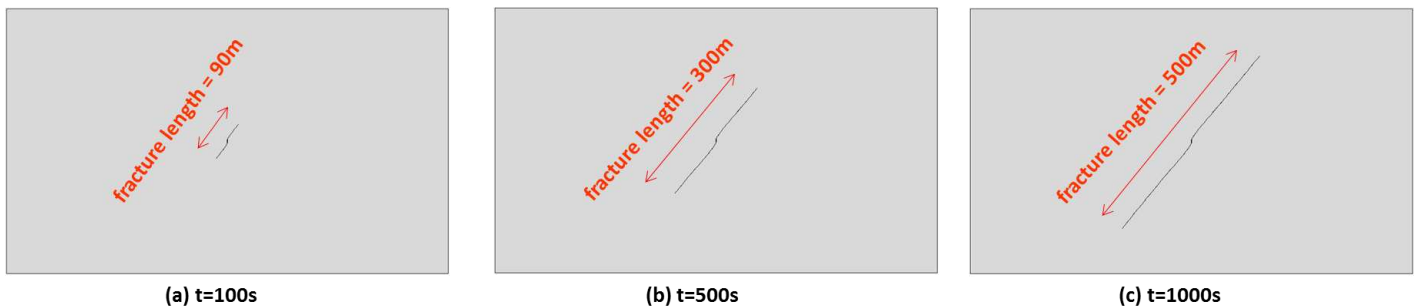


Fig. 15(a)-(c) Case 1: Propagation of hydraulic fracture

the initial stress field in the reservoir is most likely heterogeneous and this would influence the propagating fracture leading to a potentially complex fracture pathway [50] which can be modelled. Fig. 16 shows the evolution of fracture volume and length. The rate of fracture length increase is at its most rapid during the initial pumping stages and gradually reduces over the pumping schedule.

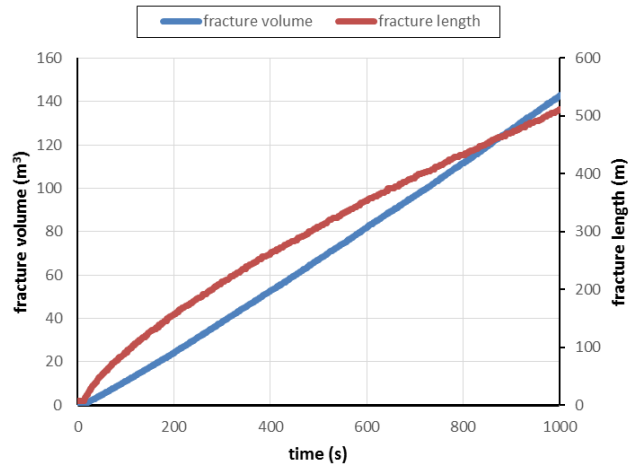


Fig. 16 Case 1: Evolution of fracture volume and fracture length

### 5.5. Case 2: Hydraulic stimulation of a naturally fractured reservoir

A key design question to the hydraulic fracture engineer is the influence of natural fractures on propagating fractures. From coring the fracture density is known in terms of the number of fractures per core length, but this provides limited information on the orientation of the natural fractures so in effect the required information is only partially known to the engineer and any remaining DFN parameters form part of a sensitivity analysis.

In this case study the exact same material properties, pre-production stresses and pumping schedules are applied as in Case 1; the only difference now being the inclusion of two DFN sets. Therefore this contrasts hydraulic fracture prediction in an intact reservoir rock with one which contains multiple DFN sets.

The evolution of the bottom hole pressure (BHP) is often analysed during the post-appraisal phase of a hydraulic fracture design to assess the accuracy of the initial model input and also to develop a better understanding of the whole fracturing process. The BHP evolution for both Case 1 (intact reservoir) and Case 2 (naturally fractured reservoir) is shown in Fig. 17. BHP starts from reservoir pressure and increases due to fluid injection and reaches a peak value, known as breakdown pressure [1], at which time the reservoir rock tensile strength is overcome and a fracture forms. Due to the sudden increase in fracture volume there is a decrease in the BHP and this eventually tends to a near constant value known as the propagating pressure. Once the fracture reaches a significant length the BHP required to maintain fracture propagation is significantly reduced; in this study the BHP drop from breakdown to propagating pressure is approximately 10 MPa.

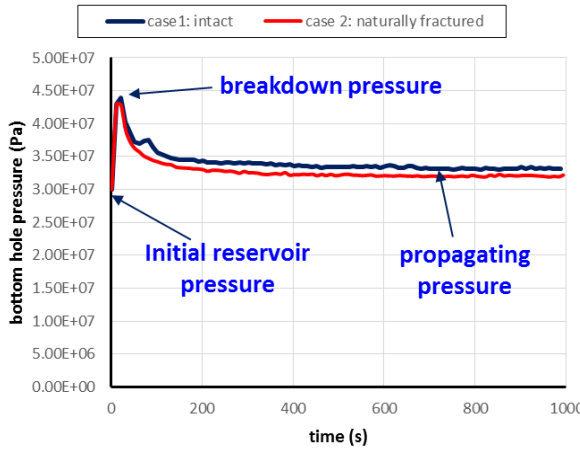


**Fig. 17 Cases 1/2: Evolution of bottom hole pressure**

Fig. 18(a)-(d) shows the evolution of the hydraulic fracture throughout hydraulic stimulation. A very important observation is the propensity of the hydraulic fracture to follow the far-field maximum horizontal principal stress direction even when connecting with natural fractures which are oblique to the initial stress state. The overriding propagating fracture direction is unchanged even though there is noticeable connectivity with both DFN sets 1 and 2. The overall fracture length is only slightly smaller than the

value computed for the intact reservoir case (compare Fig. 15(c) and Fig. 18(d)).

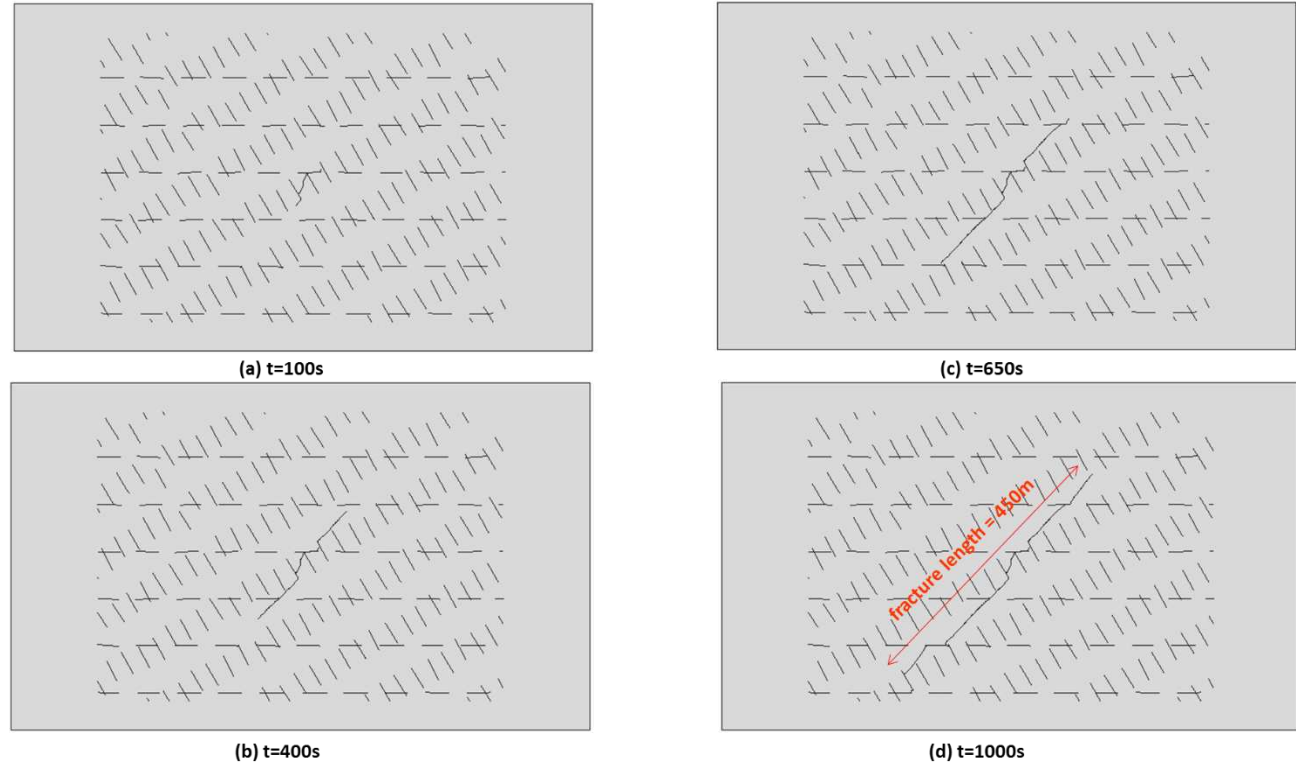
Fig. 19(a)-(b) shows the evolution of the most tensile principal stress during the initial pumping stage (i.e. t=22–32s) in a region adjacent to the stimulated section. The tip of the fracture is in tension and this allows the propagating fracture to develop and finally connect with adjacent DFN sets. The ELFEN TGR software ensures that there is a fine mesh around the tip region to adequately capture the sharp stress gradients. This is particularly important when the hydraulic fracture approaches DFN sets where large element sizes could smear out the stresses over an unduly large area and result in the propagating fracture erroneously connecting with a DFN set.

Fig. 20(a)-(b) shows the reservoir relative maximum horizontal stress  $\sigma_H^R$ , which is computed as:

$$\sigma_H^R = \frac{\sigma_H}{\sigma_H^0} \quad (27)$$

where  $\sigma_H$  and  $\sigma_H^0$  are the current and pre-production maximum horizontal stresses respectively. This parameter offers a number of insights into the mechanical behavior of the reservoir. Regions where the value is effectively equal to 1 indicates reservoir sections with unchanged stress, so it defines the limits of the stress influence of the propagating fracture. In addition, regions with perturbed values outside of 1 are very important as these can indicate whether a natural fracture is open or closed relative to its initial configuration. From Fig. 20(a)-(b) the natural fractures corresponding to DFN set 2 are in a state of increased compression (i.e.  $\sigma_H^R > 1.0$ ). This suggests that these natural fractures are now in a closed state and less conducive for porous flow, which is a key factor in obtaining sufficient hydrocarbon recovery from a gas-filled tight shale reservoir.

One of the key indicators of fracture propagation is not only the initial stress state but also the evolving stress field in terms of both magnitude and direction as the hydraulic fracture propagates in a reservoir potential populated with a high density of natural fractures. This is where numerical techniques become a powerful tool, for analyzing systems with many complex nonlinear components like continuum damage mechanics and Mohr-Coulomb frictional slip along natural fractures. Fig. 21(a)-(b) shows the evolution of the principal stress vectors near the stimulation region during the first few 10's of seconds of the pumping stage. It can be observed from Fig. 21(a) that adjacent to the propagating fracture the maximum stresses rotate such that they are orthogonal to this propagation direction. Interestingly, the extent of the rotation of the principal stresses from the initial far-field state is relatively small, so in effect only a small region surrounding the hydraulic fracture undergoes a change in stress and much of the reservoir stress remains unchanged. This is the case in point for the DFN sets, material properties and pumping schedule as defined in this paper. Further investigations are required to determine whether this observation is more universal for this class of problem.



**Fig. 18(a)-(d) Case 2: Propagation of hydraulic fracture**

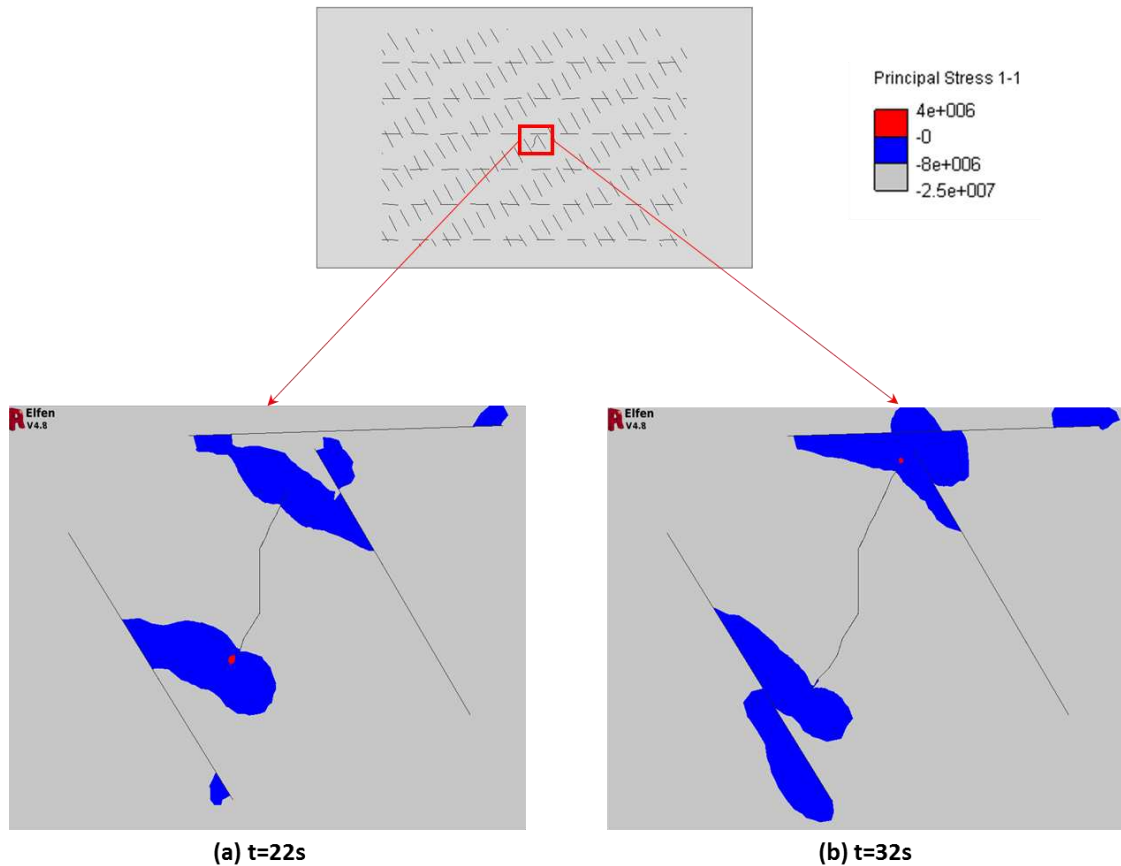


**Fig. 19(a)-(b) Case 2: Evolution of minimum principal stress (Pa) near injection region  
(positive is tensile – red contour)**

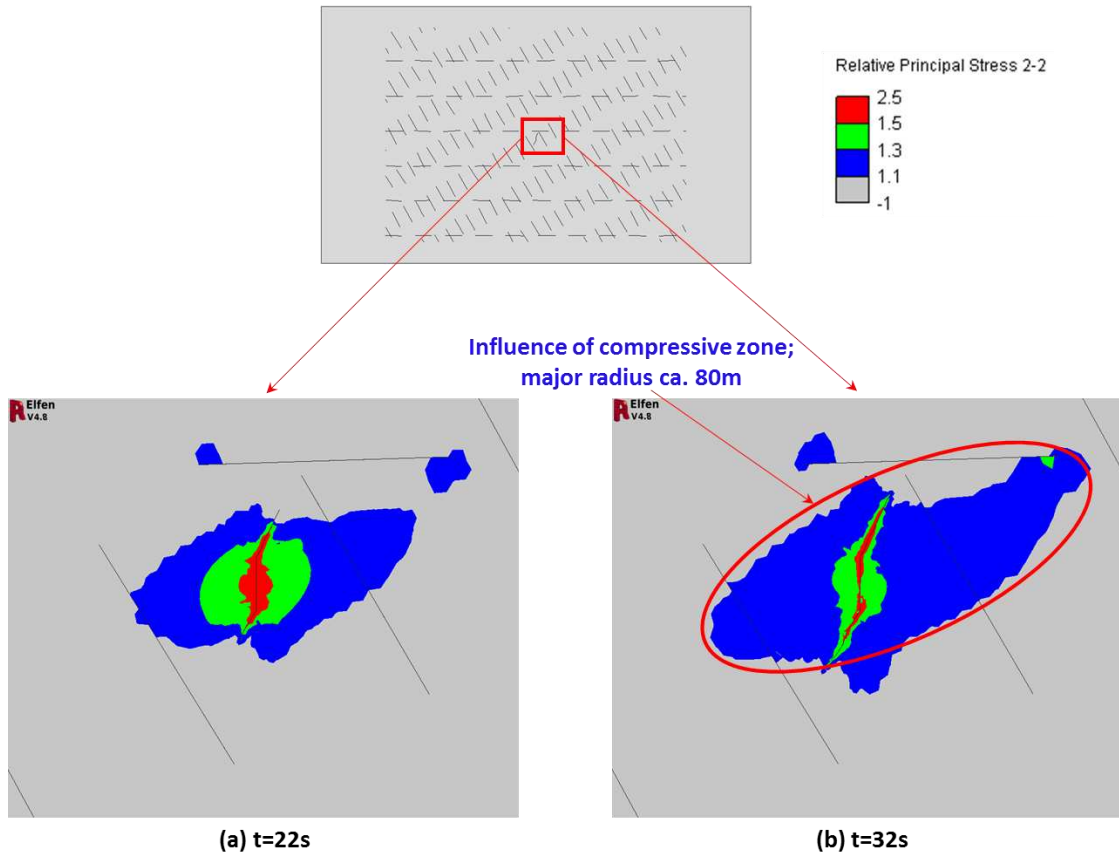


**Fig. 20(a)-(b) Case 2: Evolution of maximum horizontal principal stress near injection region  
(relative value = current value / initial value)**

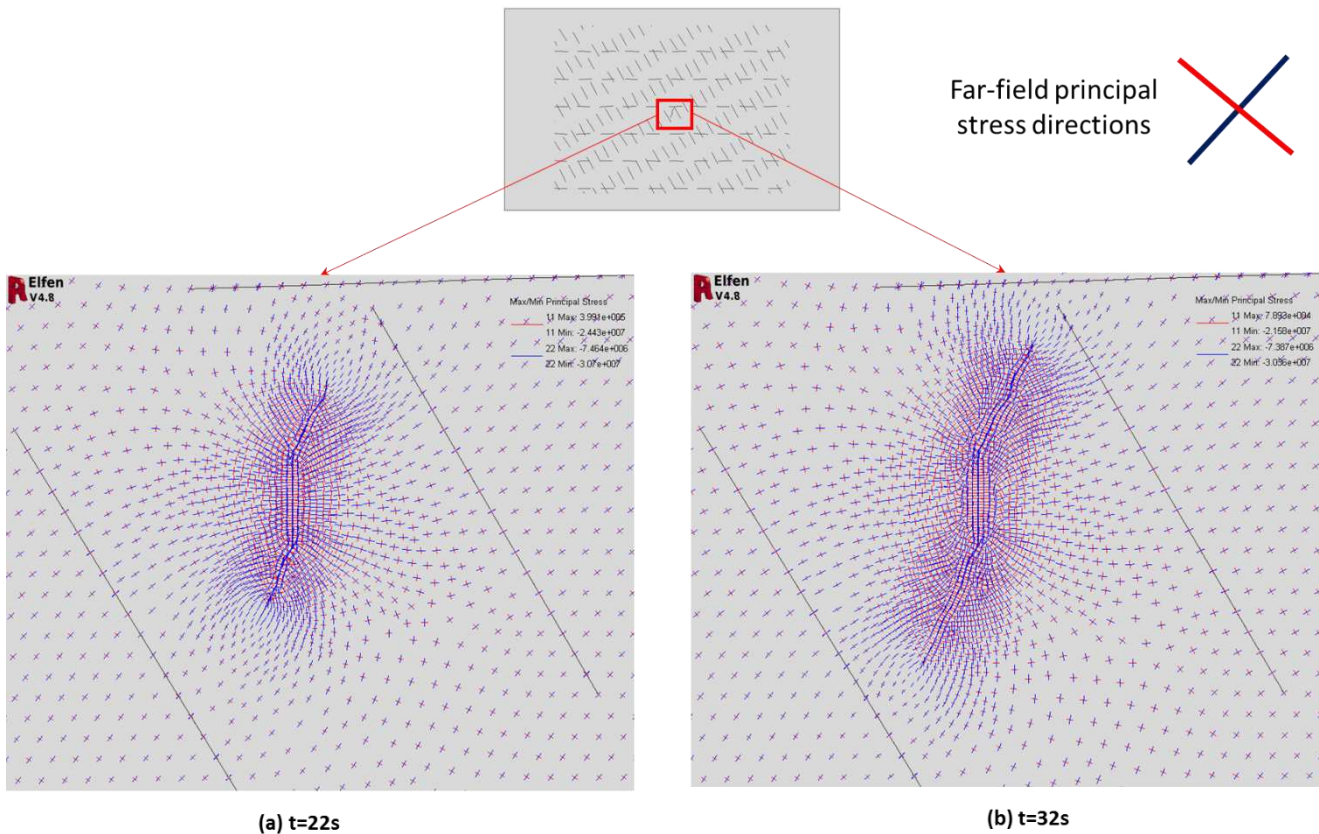


**Fig. 21(a)-(b) Case 2: Evolution of principal stress vectors (Pa) near injection region (red – minimum; blue - maximum)**

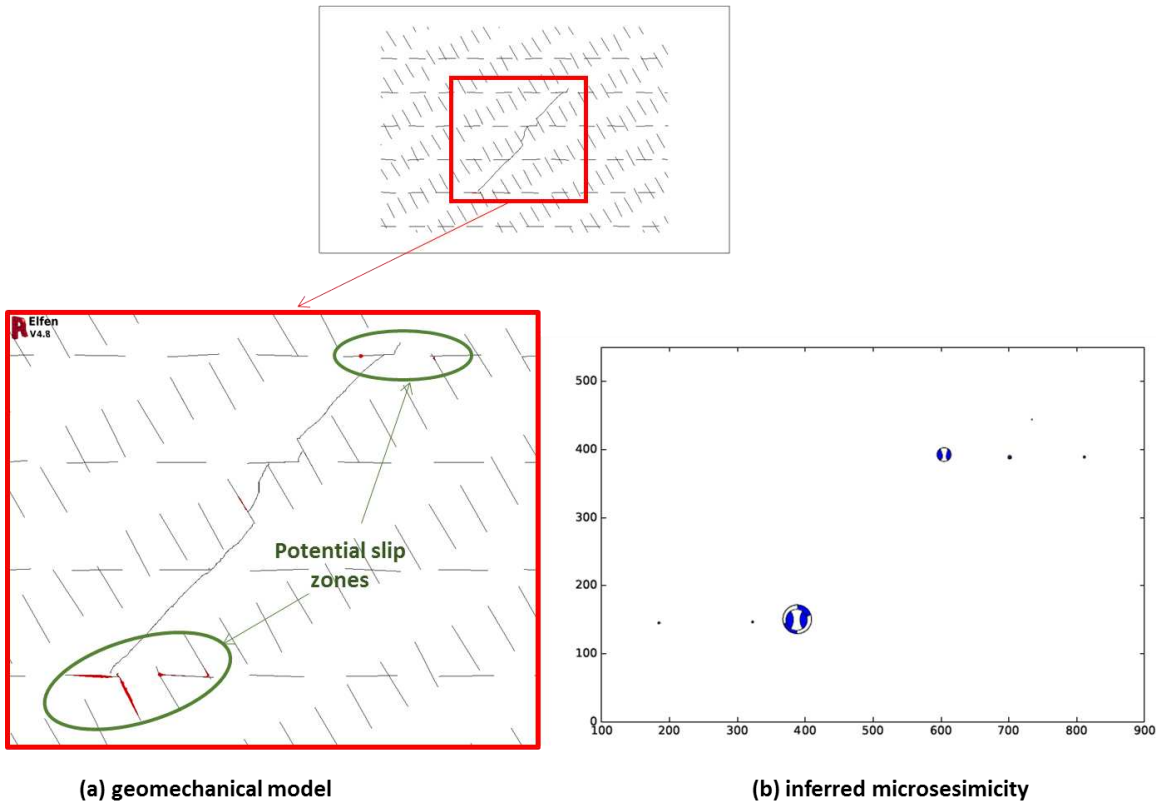


**Fig. 22(a)-(b) Case 2: link between slip prediction from geomechanical model and inferred microseismicity  
(a snapshot of the reservoir 650s after start of fluid injection)**

### 5.6. Case 2: Link between geomechanical model and microseismicity

During fluid injection the reservoir undergoes local changes in the stress field due to the propagating hydraulic fracture. As the fracture spreads into regions with a high density of DFN's it is instructive to assess the potential for slip along the surface of the DFN's. Slip results in a change of the local stress field as a new equilibrium configuration is attained. This is often referred to as the 'creaking of the rock' and the change in stress field could affect the fracture propagation direction. Fig. 22(a)-(b) shows a comparison between the slip predicted by the geomechanical model (Fig. 22(a)) and the corresponding inferred seismicity (Fig. 22(b)) 650s after pumping started. Beachballs are a graphical representation of the source mechanism [47,45] and gave information on both the potential failure mechanism in terms of seismic moments (e.g. shear or tension) and the magnitude of the seismic event. It can be observed that the stress changes remain local to the propagating fracture and do not strongly influence potential slippage along DFN sets at a distance from the fracture tip. This behaviour is confirmed from both the geomechanical model and inferred seismicity. Indeed the inferred seismicity predicts a large tensile event at the fracture tip and low shear slippage along DFN sets adjacent to the propagating fracture and this corresponds with localised stress changes observed as the fracture propagates.

## 6. Conclusions

This paper has presented a novel combined finite element and discrete element approach to investigate hydraulic

fracture stimulation in tight gas reservoirs complemented by microseismic analysis.

The method combines coupled techniques to assess the interplay between injected fluid and the mechanical response of the reservoir. The propagating fracture is a complex response combining nonlinearities at many levels, including material behaviour and the insertion of new fracture surfaces.

An innovative approach has been implemented to deal with fracture insertion based on new and dynamically updated geometrical entities rather than the traditional approach of splitting along a finite element edge. By basing fracture insertion on geometrical entities a degree of control is maintained over the quality of the evolving finite element mesh. Indeed, with the present method it was observed during an analysis that the time step size change was very small which is testament to the geometric approach.

Two demonstration cases were presented; hydraulic stimulation of both intact and naturally fracture reservoirs. The new technology was shown to predict hydraulic fractures of some 500 meters in length which is consistent with field observations by the petroleum industry. The interaction between DFN sets and far-field stresses was also shown in the naturally fractured reservoir case. In the latter case inferred microseismicity confirmed that the anticipated degree of slip along DFN sets was minimal and only those DFN sets which were near the propagating fracture were affected.

Future work for the present tool includes the capability to simulate transport of the proppant grains inside the fracture

regions (i.e. the slurry stage). This leads to a propped conductive zone inside the fracture which is required for sufficient hydrocarbon drainage of a tight gas reservoir [51].

The 2D hydraulic stimulation model presented in this paper is most suitable for thin reservoir layers and homogeneous stress states. The reservoirs are often very thin, perhaps in the region of 30-40m thick, so the 2D approximation is suitable in this instance. However, for reservoirs with highly heterogeneous stress states a 3D model is essential. The techniques described in this paper will be extended to include a fully functioning 3D hydraulic stimulation and production modelling software.

## References

1. Economides MJ, Martin T (2007) Modern fracturing enhancing natural gas production Energy Tribune
2. King GE (2010) Thirty years of gas shale fracturing: what have we learned? Proceedings of the SPE Annual Technical Conference and Exhibition held in Florence Italy 19-22 September SPE 133456
3. Cipolla CL, Lolon EP, Erdle JC, Rubin B (2010) Reservoir modelling in shale-gas reservoirs Proceedings of the SPE Eastern region Meeting held in Charleston, West Virginia USA 23-25 September SPE 15530
4. Khoei AR (2015) Extended finite element method: theory and applications Wiley
5. Economides MJ, Nolte KG (2000) Reservoir stimulation Wiley
6. Matthews HL, Schein G, Malone M (2007) Simulation of gas shales; they're all the same – right? Proceedings of the Hydraulic Fracturing Technology Conference held in College Station, Texas USA 29-31 January SPE 106070
7. Mayerhofer MJ, Lolon EP, Warpinski NR, Cipolla CL, Walser D, Rightmire CM (2008) What is stimulated reservoir volume? Proceedings of the Shale Gas Production Conference held in Fort Worth, Texas USA 16-18 November SPE 119890
8. Jones J, Britt JZ (2005) Design and appraisal of hydraulic fractures Society of Petroleum Engineers
9. Yew CH, Weng X (2015) Mechanics of hydraulic fracturing Gulf Professional Publishing
10. Belytschko T, Liu WK, Moran B (2000) Nonlinear finite elements for continua and structures Wiley
11. Wu SR, Gu L (2012) Introduction to the explicit finite element method for nonlinear transient dynamics Wiley
12. Alqahtani NB, Miskimins JL (2010) 3D finite element modeling of laboratory hydraulic fracture experiments Proceedings of the Annual Conference held in Barcelona, Spain 14-17 June SPE 130556
13. Nassir M, Settari A, Wan H (2012) Prediction and optimization of fracturing in tight gas and shale using a coupled geomechanical model of combined tensile and shear fracturing Hydraulic Fracture Technology Conference in The Woodlands, Texas, USA, 6-8 February SPE 152200
14. Cipolla CL, Warpinski NR, Mayerhofer MJ, Lolon EP, Vincent MC (2010) The relationship between fracture complexity, reservoir properties and fracture-treatment design Annual Technical Conference and Exhibition, Denver, Colorado, USA 21-24 September SPE 115769
15. Weng X, Kresse O, Cohen C, Wu R, Gu H (2011) Modeling of hydraulic-fracture-network propagation in a naturally fractured formation Hydraulic Fracturing Technology Conference in The Woodlands, Texas, USA, 24-26 January SPE 140253
16. Kresse O, Cohen C, Weng X, Wu R, Gu H (2011) Numerical modeling of hydraulic fracturing in naturally fractured formations 45th US Rock Mechanic / Geomechanics Symposium in San Francisco, CA, June 26-29
17. McClure MC (2012) Modeling and characterization of hydraulic stimulation and induced seismicity in geothermal and shale gas reservoirs Ph.D. thesis Stanford University
18. Munjiza A (2004) FEFLOW: Combined finite-discrete element method Wiley
19. Gordeliy E, Peirce A (2013) Coupling schemes for modelling hydraulic fracture propagation using the XFEM. Comput Method Appl M 253:305-322
20. Lisjak A, Liu Q, Zhao Q, Mahabadi OK, Grasselli G (2013) Numerical simulation of acoustic emission in brittle rocks by two-dimensional finite-discrete element analysis. Geophys J Int 195:423-443
21. Kolditz O, Delfs J-O, Burger C, Beinhorn M, Park C-H (2008) Numerical analysis of coupled hydrosystems based on an objected compartment approach J. Hydroinform. 10: 227-244
22. Kolditz O, Gorke U-J, Shao H, Wang W (2012) Thermo-hydro-mechanical-chemical processes in fractured porous media Springer
23. Wang W, Kolditz O 2004, Object-oriented finite element analysis of thermos-hydro-mechanical (THM) problems in porous media Int. J. Numer. Engng. 69:162-201
24. ELFEN TGR Manual (2014) Rockfield Software Ltd
25. Kim J (2010) Sequential methods for coupled geomechanics and multiphase. Ph.D. thesis Stanford University
26. Bai M, Elsworth D (2000) Coupled processes in subsurface deformation, flow, and transport ASCE Press
27. Diersch HJ (2013) FEFLOW: Finite element modeling of flow, mass and heat transport in porous and fractured media Springer
28. Lobao MC (2007) Finite element modelling of hydraulic fracture flow in porous media. Ph.D. thesis Swansea University
29. Valko P, Economides MJ (1995) Hydraulic fracture mechanics Wiley

30. Lewis RW, Schrefler JZ (1998) The finite element method in the static and dynamic deformation and consolidation of porous media Wiley
31. Klerck PA (2000) The finite element modelling of discrete fracture in quasi-brittle materials. Ph.D. thesis Swansea University
32. Bazant PZ, Planas J (1997) Fracture size effect in concrete and other quasi-brittle mateirals CRC Press
33. Crook AJL, Willson SM, Yu JG, Owen DRJ (2006) Predictive modelling of structure evolution in sandbox experiments. *Journal of Structural Geology* 28:729-744
34. Crook T, Willson S, Yu JG, Owen R (2003) Computational modelling of the localized deformation associated with borehole breakout in quasi-brittle materials. *J Petrol Sci Eng* 38:177-186
35. Bai M (2011) Improved understanding of fracturing tight-shale gas formations Proceedings of the Production and Operation Symposium held in Oklahoma City, Oklahoma 27-29 March SPE 140968
36. Williams BB (1970) Fluid loss from hydraulically induced fractures. *J Pet Tech* 22:882-888
37. Zienkiewicz OC, Taylor RL, Zhu JZ (2005) The finite element method: its basis and fundamentals Butterworth-Heinemann
38. Huang M, Yue ZQ, Tham LG, Zienkiewicz OC (2004) On the stable finite element procedures for dynamic problems of saturated porous media. *Int J Numer Meth Engng* 61:1421-1450
39. Minkoff SE, Stone CM, Bryant S, Peszynska M, Wheeler MF (2003) Coupled fluid flow and geomechanical deformation modeling. *J Petrol Sci Eng* 38:37-56
40. Huang M, Wu S, Zienkiewicz OC (2001) Incompressible or nearly incompressible soil dynamic behaviour – a new staggered algorithm to circumvent restrictions of mixed formulation. *Soil Dyn Earthq Eng* 21:169-179
41. Barree RD, Gilbert JV (2009) Stress and rock property profiling for unconventional reservoir stimulation Proceedings of the Hydraulic Fracturing Technology Conference held in The Woodlands, Texas USA 19-21 January SPE 118703
42. Olovsson L, Simonsson K, Unosson M (2005) Selective mass scaling for explicit finite element analyses. *Int J Numer Meth Engng* 63:1436-1445
43. Davies RJ, Mathias S, Moss J, Hustoft S, Newport L (2012) Hydraulic fractures: how far can they go? *Mar Petrol Geol* 37:1-6
44. Peric D, Hochard CH, Dutko M, Owen DRJ (1996) Transfer operators for evolving meshes in small strain elasto-plasticity *Comput. Methods Appl. Mech. Engrg.* 137: 331-344
45. Angus DA, Kendall JM, Fisher QJ, Segura JM, Skachkov S, Crook AJL, Dutko M (2010) Modelling microseismicity if a producing reservoir from coupled fluid-flow and geomechanical simulation. *Geophys Prospect* 58:901-914
46. Hazzard J, Young R (2002) Moment tensors and micromechanical models, *Tectonophysics*, 356: 181–197
47. Angus DA, Dutko M, Fisher QJ, Kendall JM, Kristiansen TG, Barkved OI, Yu J, Zhao S (2013) Integrated hydro-mechanical and seismic modelling of the Valhall reservoir: predicting subsidence, AVOA and microsesimicity International Workshop on Geomechanics and Energy – The Ground as Energy Source and Storage held in Lausanne, Switzerland 26-28 November
48. Wriggers P (2006) Computational contact mechanics Springer
49. Zhong ZH (1993) Finite element procedures for contact-impact problems Oxford University Press
50. Soliman MY, Augustine J (2010) Fracturing design aimed at enhancing fracture complexity Proceedings of the Annual Conference held in Barcelona, Spain 14-17 June SPE 130043
51. Medeiros F, Ozkan E, Kazemi H (2008) Productivity and drainage area of fractured horizontal wells in tight gas reservoirs Proceedings of the Rocky Mountain Oil and Gas Technology Symposium held in Denver, Colorado USA 16-18 April SPE 108110